Visualising Plating-Induced Cracking in Lithium Anode Solid Electrolyte Cells

Ziyang Ning[1], Dominic Spencer Jolly[1], Guanchen Li[3,4], Robin De Meyere[1], Shengda D. Pu[1], Yang Chen[1], Jitti Kasemchainan[1,3], Johannes Ihli[5], Chen Gong[1], Boyang Liu[1,3], Dominic Melvin[1,3], Anne Bonnin[5], Oxana Magdysyuk[6], Paul Adamson[1,3], Gareth O. Hartley[1,3], Charles W. Monroe[3,4], T. James Marrow[1], Peter G. Bruce[1,2,3]

1. Department of Materials. University of Oxford, Oxford, UK
2. Department of Chemistry, University of Oxford, Oxford, UK
3. The Faraday Institution, Harwell Campus, Didcot, UK
4. Department of Engineering Science, University of Oxford, Oxford, UK
5. Paul Scherrer Institut, Villigen PSI, Switzerland
6. Diamond Light Source, Harwell Campus, Didcot, UK

Abstract

Lithium dendrite (filament) propagation through ceramic electrolytes, leading to short-circuits at high rates of charge, is one of the greatest barriers to realising high energy density all-solid-state lithium anode batteries. Utilising *in-situ* X-ray computed tomography coupled with spatially mapped X-ray diffraction, the propagation of cracks and the propagation of lithium dendrites through the solid electrolyte have been tracked in a Li/Li_6PS_5Cl/Li cell as a function of the charge passed. On plating, cracking initiates with spallation, conical “pothole”-like cracks that form in the ceramic electrolyte near the surface with the plated electrode. The spallations form predominantly at the lithium electrode edges where local fields are high. Transverse cracks then propagate from the spallations across the electrolyte from the plated to the stripped electrode. Lithium ingress drives the propagation of the spallation and transverse cracks by widening the crack from the rear, i.e. the crack front propagates ahead of the Li. As a result, cracks traverse the entire electrolyte before the Li arrives at the other electrode and therefore before a short-circuit occurs.

Introduction

Solid-state batteries with lithium metal anodes and ceramic electrolytes are of intense current interest as they could deliver a step change in energy density, as well as improved safety compared with today’s lithium-ion batteries[1–3]. The inability to plate lithium metal on charging at practical current densities without the metal penetrating the ceramic electrolyte and leading to a short-circuit is one of the greatest barriers to progress[4–15]. Previous work has shown that dendrite growth through polymer electrolytes is suppressed if the electrolyte has a sufficiently high shear modulus[16,17]. However, ceramics with orders of magnitude higher shear moduli than lithium do not supress dendrite growth, demonstrating that the mechanism for dendrite penetration through ceramics is different from that through polymers and is as yet not well understood.

Ex-situ and destructive methods, involving sectioning the ceramic electrolyte and imaging the lithium metal within using techniques such as scanning electron microscopy, have proved

valuable in demonstrating the problem[18–21]. However, it is important to follow the development of cracks and the ingress of lithium metal into the ceramic during operation of the cell in order to understand the mechanism of dendrite penetration and cell failure. Optical microscopy has been used for *in-situ* studies. However, it is challenging to characterise dendrites buried inside the solid electrolyte[22–24]. X-ray computed tomography (XCT) carried out during all-solid-state battery operation has imaged the evolution of interfacial voids and has been used to follow the growth of reactive interphase layers when Li is contacted with $Li_{1+x}Al_xGe_{2-x}(PO4)_3$ (LAGP), where the growing interphase results in electrolyte cracking[25–30].

In this study, we use *in-situ* XCT with high spatial resolution and phase-contrast, combined with spatially mapped X-ray diffraction, which enables us to follow the progression of cracks and the progression of the lithium ingress as a function of charge passed in cells composed of argyrodite solid electrolyte (Li_6PS_5Cl) sandwiched between two lithium metal electrodes. This sulphur-based electrolyte is a strong candidate for all-solid-state batteries and is a useful model system because it combines high conductivity with the ability to form a stabilising solid electrolyte interface (SEI) of a few nm in contact with lithium metal[31–35]. This makes Li_6PS_5Cl, in contrast to LAGP, a good case for studying electrolyte fracture as there is no continuous formation of an interphase that grows through the solid electrolyte with associated volume change and therefore electrolyte cracking in the case of Li_6PS_5Cl can be attributed to lithium plating.

By tracking *in-situ* both lithium ingress and crack propagation into the ceramic, we show that the crack front propagates well ahead of metallic lithium in the crack. On plating lithium, spallations (conical “pothole”-like cracks) form in the electrolyte adjacent to the plated electrode. The spallation crack propagates towards the plated electrode surface along a path where porosity is above the average of the ceramic. They are also more prevalent at the edges of the lithium electrode due to higher local field and current density. Transverse cracks emanate from the spallations and propagate across the electrolyte, forming a path between the plated and stripped electrodes. Lithium ingress drives the propagation of the spallation and transverse cracks by widening the crack from the rear, i.e. the crack front propagates ahead of the Li and Li is not at the crack tip. Only later when lithium plates along the entire crack does the cell finally short circuit.

Spallation in the ceramic electrolyte at the interface with the plated lithium electrode

A pressure-controlled, two-electrode symmetric Li/Li_6PS_5Cl/Li cell was assembled without exposure to air and was mounted in a synchrotron XCT beamline using a loading rig. Galvanostatic cycling was performed under a compression of 7 MPa at a current density of 1.25 mA cm^{-2} for a capacity of 0.5 mAh cm^{-2}, Fig. 1. High current density, that results in high overpotential, was used to ensure Li dendrite formation and electrolyte cracking during cycling. XCT image slices were acquired along planes parallel to, and 5 pixels (8.15 µm) from, the two Li/solid electrolyte interfaces, Fig. 1b; the positions of the image slices in Fig. 1b are indicated by the red and blue arrows on the virtual cross-sectional image slice in Fig. 1c(i). The light grey disks at the centre of the XCT scans in Fig. 1b are manually superimposed onto the image slices to mark the position of the lithium electrodes. Images were collected before cycling, after the first half cycle and after successive full cycles. The cycling commenced with

plating (lithium deposition) occurring at the interface shown in Fig. 1b(i) and with stripping occurring at the interface shown in Fig. 1b(ii). Before cycling, there was no evidence of cracks pre-existing in the electrolyte in the proximity of either interface with lithium, Fig. 1b(i) & (ii). After one half cycle, the interface that underwent stripping remained largely unchanged, Fig. 1b(iv); whereas cracks were clearly observed in the solid electrolyte adjacent to the electrode interface which underwent plating, Fig. 1b(iii). The cracks observed in the ceramic, in the proximity of the plated electrode, were more prevalent close to the edge of the lithium electrode as compared with the central region. As the formation of these cracks was observed to be a plating-induced phenomenon, we focused on the first-plated electrode for observation of the evolution of the process during subsequent cycles. Image slices, adjacent to the electrode which was plated first, are shown in Fig. 1b after the (v) 2^{nd}, (vi) 3^{rd}, (vii), 4^{th}, and (viii) 5^{th} plating steps. Similar cracks of larger quantity and dimensions were observed to arise with each successive cycle, while the edge-preferred distribution of the cracks remained apparent. A gradual decrease in the magnitude of cell polarization, starting from the second cycle, was seen during cycling, Fig. 1a, and voltage spikes were detected on the 2^{nd} and 3^{rd} charge. Such voltage responses have been observed and their origins discussed in previous studies of lithium ingress into ceramic electrolytes[36,37]. To understand how these cracks affect the impedance of the cell, electrochemical impedance spectroscopy (EIS) was conducted on the pristine cell and after every plating of the first plated electrode. These data, shown in Fig. S2, demonstrate a gradual decrease in cell impedance as the number of these cracks increases, providing evidence that lithium ingresses into these cracks, increasing the contact area between lithium and the ceramic electrolyte. A virtual cross-sectional image slice of the cell, Fig. 1c(i), was taken orthogonal to the Li/Li_6PS_5Cl interface at the position indicated by the dashed red line in Fig. 1b(iii). The virtual cross-sectional image shows that the cracks near the plated electrode are cone-shaped sections of electrolyte that have become largely detached from the bulk electrolyte, in the case of the crack highlighted in Fig. 1c it is in the region of 100 microns into the electrolyte. Due to their geometric similarity to pothole-like spallation cracks observed in surface damage of concrete and other brittle ceramics, the features formed are termed, *spallations*. The virtual cross-sectional images in Fig. 1c(i) and (iii), reinforce the preference for spallations at the edges of the lithium electrode. On the virtual cross-sectional slice, Fig. 1c(iii), a vertical crack can be seen to propagate from underneath the spallation, which suggests a correlation between spallation and vertical cracking. The latter phenomenon is associated directly with final battery failure, as discussed below. A magnified image from the cross-sectional image slice of the pristine cell was taken at the same position of c(iii), showing no pre-existing defects, Fig. c(ii). It should be noted that spallations are not limited to Li/Li_6PS_5Cl cells; they are also observed in cycled Li/Li_3N cells, Fig. 1d and Fig. S4, and cycled Na/Na-beta''-Alumina cells (Fig. S3). Li_3N and Na-beta''-Alumina have been shown to be chemically unreactive with their respective anodes, thus the formation of spallation and vertical cracks do not rely on the formation of an interphase layer[38,39]. Furthermore, virtual cross-sectional images of a different spallation show cracking initiating in the Li_6PS_5Cl electrolyte ~20 µm below the surface with the plated electrode (Fig. S5). The SEI layer that forms at the Li/ Li_6PS_5Cl interface self-limits at a few nm[33], a very different length scale from the spallations. These cracks are therefore unlike those observed in LAGP, where the interphase layer grows continuously across the electrolyte and cracking has been attributed

to the associated strain. Li_6PS_5Cl, Li_3N and Na-beta''-Alumina are very different electrolytes and yet the same behaviour applies, suggesting that spallation is a general phenomenon in solid-state batteries with metallic electrodes. *Ex-situ* SEM carried out on a (physically) cross-sectioned, cycled Li/Li_6PS_5Cl/Li cell confirmed the presence of spallation features (Fig. S6.).

The spallation crack formation and in particular the response of the crack to plating and stripping, was followed in more detail by digital volume correlation (DVC). DVC tracks the changes in the position of sub-volumes of the images by comparing the *in-situ* phase-contrast XCT scans of the pristine and cycled cells. The DVC generates a 3D displacement field from the movement of the sub-volumes. A strain field is then obtained by calculating the gradient of the displacement field[40].

The maximum 3D strain at each point on the image slice adjacent and parallel to the plated electrode is shown in Fig. 2, the colour represents the intensity of the strain at each point. Hot spots of positive strain are seen as lithium deposition results in the spalling-out (detachment) of the electrolyte and the spallation crack widens. Positive strains are most prevalent around the edge of electrode after plating in areas where spallations exist or newly emerge. Such positive strains reduced as lithium was stripped back. With cycling there is a net accumulation of strain and spallation cracks, Fig. 2.

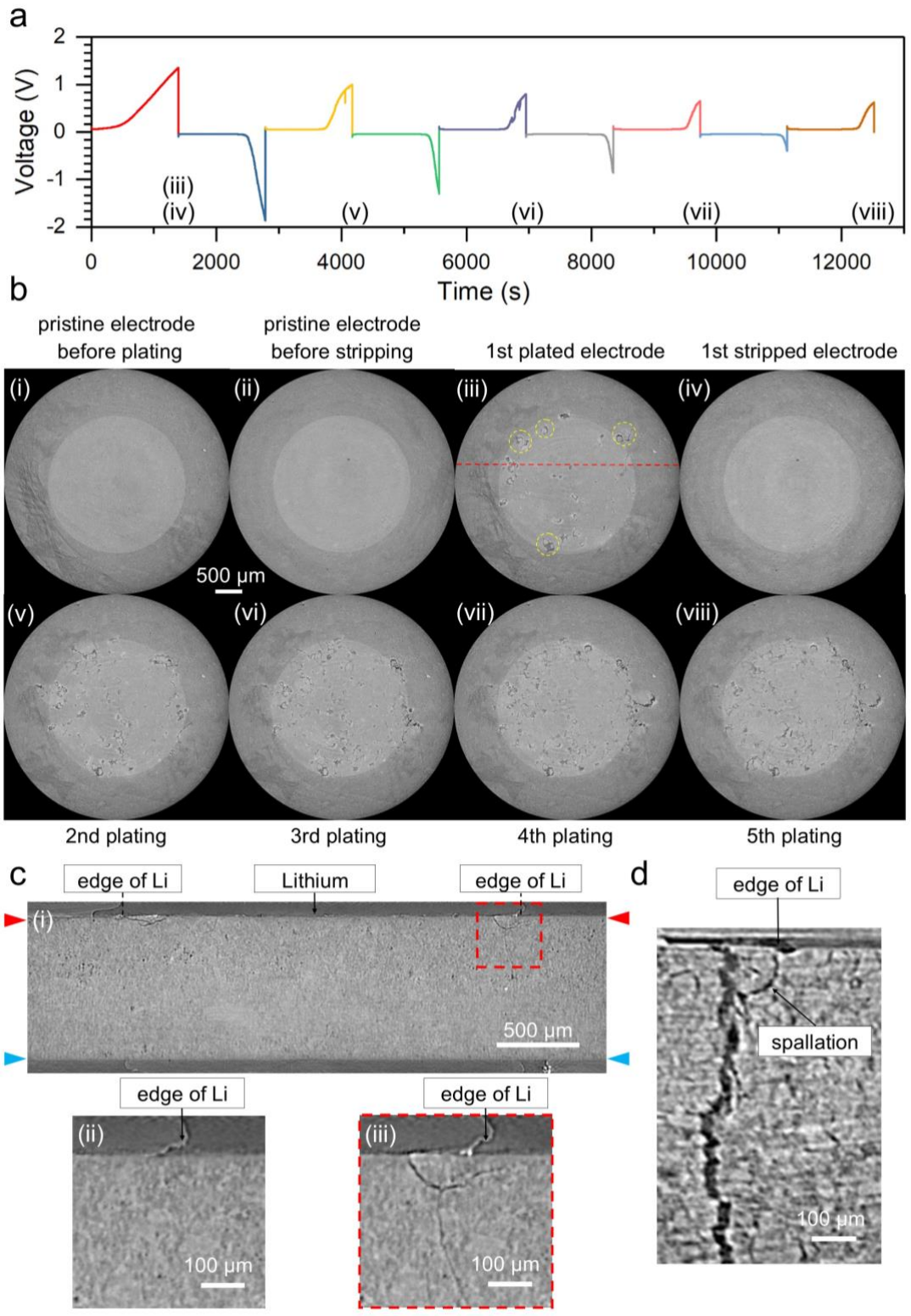

Fig. 1. *In-situ* phase-contrast X-ray CT of a Li/Li_6PS_5Cl/Li cell showing lithium plating-induced spallation. a. voltage versus time for the symmetric Li/Li_6PS_5Cl/Li cell cycled at 7 MPa, 1.25 mA cm^{-2}, with a capacity of 0.5 mAh cm^{-2}. Each colour represents half a cycle. The

numbers correspond to the different stages of cycling at which X-ray CT scans shown in b (iii) to (viii) were collected. **b**. virtual image slices taken along planes parallel to and at 5 pixels (8.15 µm) beneath each lithium electrode (positions indicated by red and blue arrows in c.). (i) and (ii) are slices taken at the electrodes to be (i) plated and (ii) stripped, before passing a current; (iii) plated interface and (iv) stripped interface, after the first half cycle; (v) to (viii) show the evolution of the 1st interface to be plated, after successive cycles. Light grey disks were superimposed onto the virtual image slices to mark the position of lithium electrodes. **c**. (i) cross-sectional image slice along the red dashed line in b(iii) reveals the spallations at the edge of the lithium electrode and 100 microns into the electrolyte. (ii) A magnified image from the cross-sectional image slice of the pristine cell at the position of c(iii), showing no pre-existing defects. (iii) A magnified image shows a vertical crack under spallation, indicating correlation between spallation and vertical cracking. The wave like feature on the right-hand side of the Li electrode corresponds to the edge of Li metal where it contacts with the polymer insulating ring used to constrain and define the footprint of the Li electrode. **d.** cross-sectional image slice taken from X-ray CT scan of cycled Li/Li_3N/Li symmetric cell, showing a spallation at the edge of the lithium electrode, and a vertical crack under the spallation.

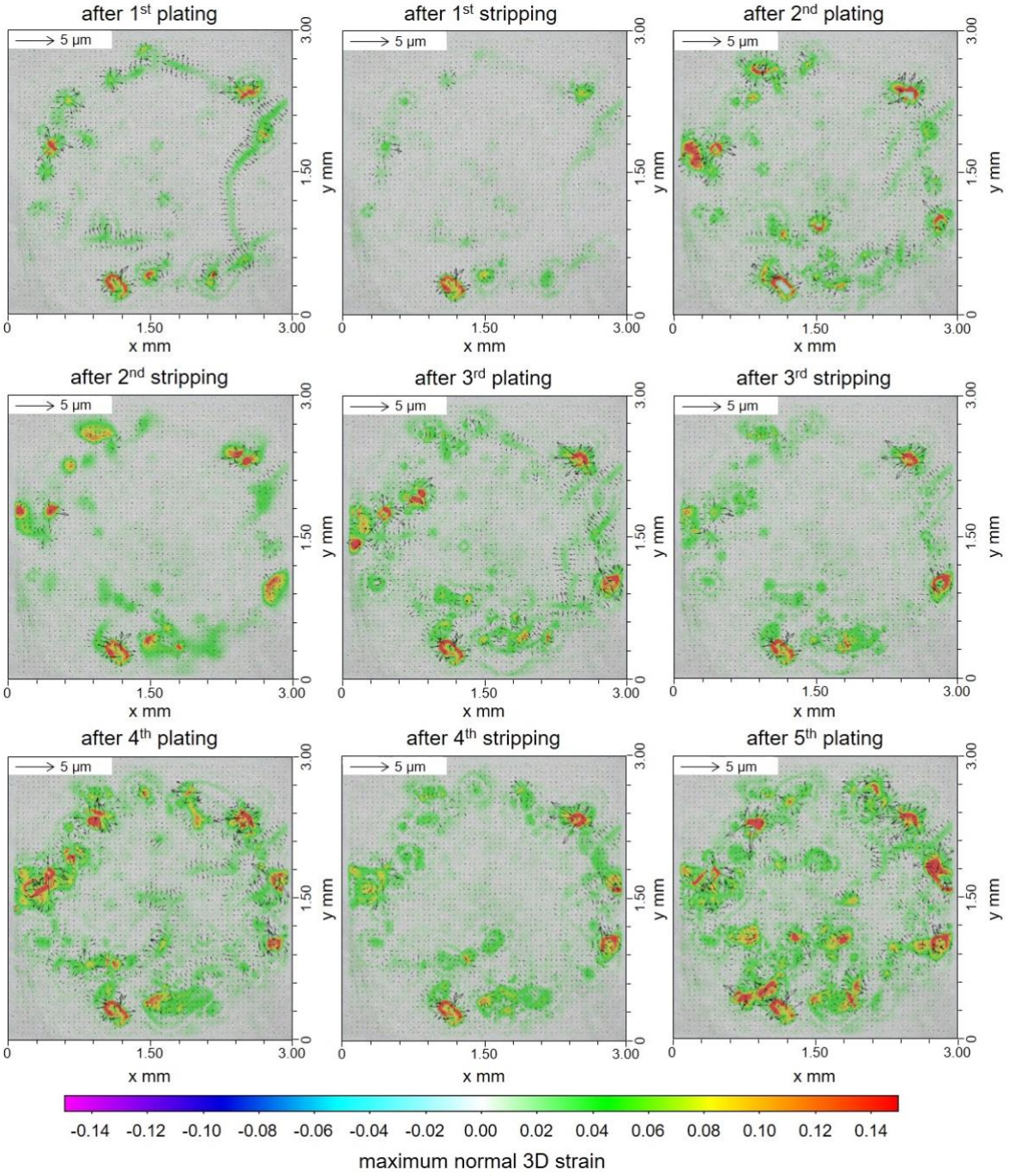

Fig. 2. Images from a plane parallel and adjacent to the plated electrode showing the maps of maximum normal 3D strain at each point on the plane (colour map) and displacement (arrows) of the electrolyte at different stages of cycling, obtained from digital volume correlation (DVC) analysis of the *in-situ* X-ray CT scans.

Crack propagation and lithium penetration into the electrolyte during plating

As phase-contrast imaging with a highly coherent beam can effectively enhance the contrast of weakly attenuating materials[41,42], i.e. lithium, we are able to reliably distinguish deposited lithium from the empty space created by crack propagation. In order to track the propagation

of cracks and their relation to lithium propagation into the solid electrolyte during plating, further *in-situ* XCT was performed on a Li/Li_6PS_5Cl/Li cell as a function of the charge passed, Fig. 3. Fig. 3a shows a series of virtual cross-sectional image slices, taken from the same position in the cell: (i) before passing a current, and after plating with (ii) 0.2 mAh cm^{-2}, (iii) 0.4 mAh cm^{-2}, (iv) 0.6 mAh cm^{-2}, (v) 0.8 mAh cm^{-2}, and (vi) 1.0 mAh cm^{-2} of lithium. The greyscale intensity in the tomographic images depends on the electron density of the constituent atoms[43]; here, lighter grey corresponds to heavier atoms and black corresponds to empty space. Fig. 3b shows magnified images of the electrolyte region near the plated electrode where the crack develops. After passing 0.2 mAh cm^{-2} of charge, a crack forms in the solid electrolyte underneath the electrode (as can be seen in the top right of the image in Fig. 3b(ii)). After 0.4 mAh cm^{-2} of charge, a spallation becomes apparent. In addition, the formation of a crack perpendicular to the electrode is observed (vertical crack), which with increasing charge passed, advances towards the stripped (bottom) electrode. Both the spallation crack and the vertical crack lengthen and widen with increasing charge passed, Fig. 3a and b (iii) to (vi). After 0.8 mAh cm^{-2}, the vertical crack propagates through the entire thickness of the Li_6PS_5Cl disk and reaches the stripped electrode at the bottom. The voltage of the cell as a function of charge passed is shown in Fig. 3c. There is no evidence of a short-circuit. The absence of a short-circuit, even after the passage of 1.0 mAh cm^{-2} of charge, implies that lithium did not propagate across the solid electrolyte, despite the crack having done so.

To study the propagation of lithium into the electrolyte, the grayscale intensity was examined in both the spallation and vertical cracks. As an empty crack presents zero X-ray attenuation, the grayscale value increases with the amount of lithium within the image voxels that are in the crack. First, the extent of lithium ingress into the spallation crack was assessed by analysing the grayscale across the crack along the red line in Fig. 3a and b (iii) to (vi). These results are shown in Fig. 3d. With the passage of charge a gradual increase of attenuation is observed, which corresponds to increasing lithium deposition in the crack. The continuous grayscale inside the crack and the dynamic growth as more charge is passed excludes the possibility that the attenuating phase inside the crack is fragmented ceramic electrolyte, showing that it is indeed lithium deposition being observed. To examine lithium propagation along the vertical crack, the grayscale values were determined at the two regions of the crack shown with blue and yellow boxes, and were compared with that of the spallation crack shown with the red box, Fig. 3e. The attenuation near the top of the vertical crack (blue box) and the lack of attenuation lower down the crack (yellow box), confirm that although the crack has propagated across the whole electrolyte after passage of 1.0 mAh cm^{-2}, only the top of the vertical crack, close to the plated electrode, is occupied by lithium, Fig. 3f. In addition, continuous grayscale analysis was conducted from inside the vertical crack to inside the spallation crack, showing a continuous increase in the average attenuation coefficient towards the plated electrode, showing that lithium is propagating along the crack, Fig. S7. Overall, the grayscale analysis shows that after 0.8 mAh cm^{-2} lithium is filling the spallation crack and that after 1.0 mAh cm^{-2} there is lithium only at the top of the vertical crack, yet the crack has traversed the entire electrolyte between the two electrodes. Lithium ingress (dendrites) drives the formation and propagation of spallation and transverse cracking in the solid electrolyte, and crucially from far behind the crack tip. Lithium ingress partially fills the crack widening it and leading to crack propagation ahead of the Li. In other words, Li drives crack propagation

from the rear not at the crack tip. The transverse crack reached the other electrode before the Li, only later does the Li arrive and causes short-circuit.

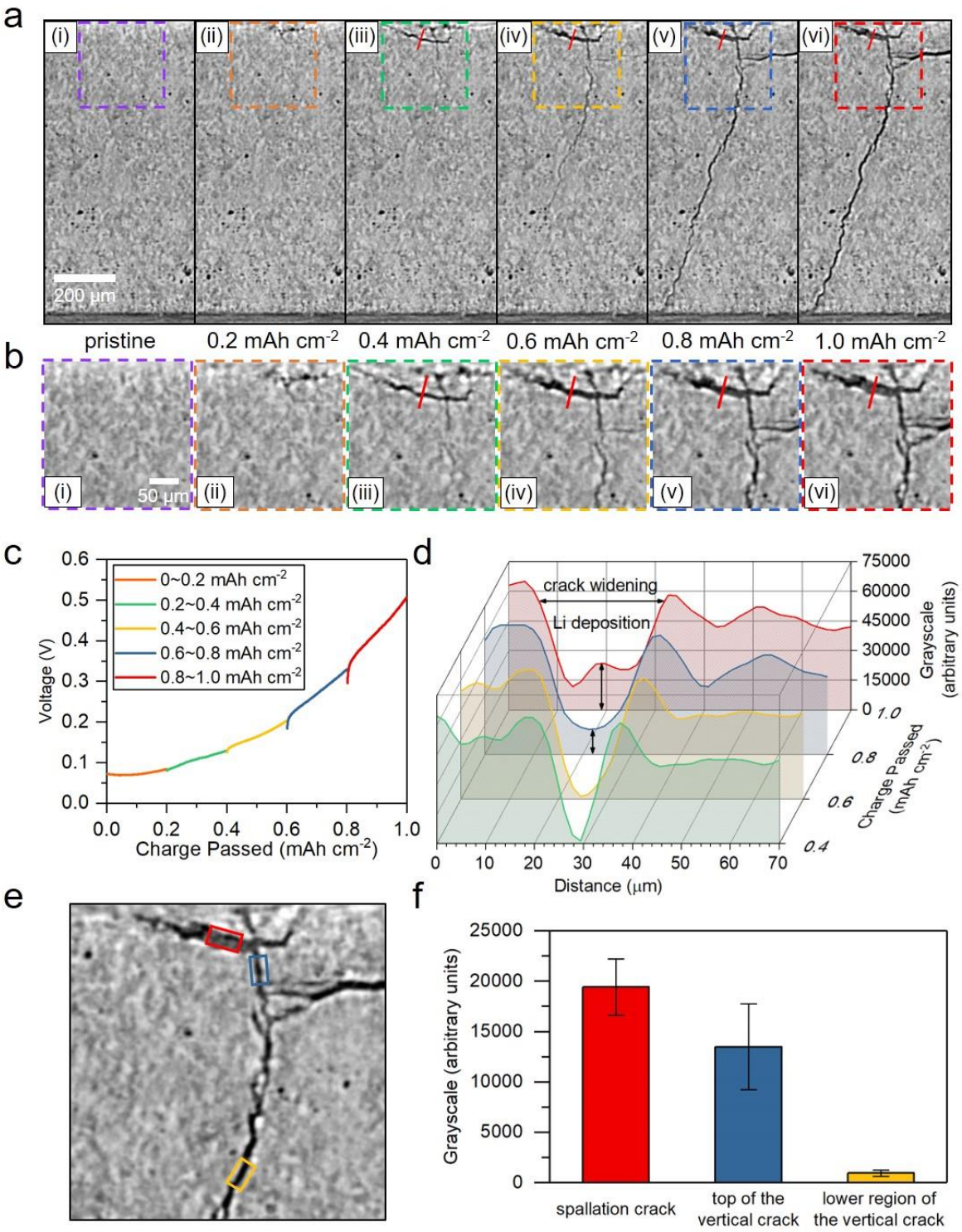

Fig. 3. *In-situ* phase-contrast X-ray CT virtual cross-sections during a single plating of a Li/Li_6PS_5Cl/Li cell and analysis of lithium deposition in the cracks showing that cracks propagate ahead of Li a. virtual cross-sectional image slices of (i) the pristine cell and after (ii) 0.2 mAh cm^{-2}, (iii) 0.4 mAh cm^{-2}, (iv) 0.6 mAh cm^{-2}, (v) 0.8 mAh cm^{-2} and (vi) 1.0 mAh cm^{-}

^{2} of charge passed, plated electrode at the top. **b**. magnified images of the regions defined by the boxes in a (i) to (vi). **c**. voltage versus charge passed showing increasing polarisation and no short-circuit (no sudden drop in voltage) even when the crack has propagated across the entire electrolyte. **d**. measured grayscale profiles across the crack at the region indicated by the red line in b. showing the accumulation of lithium inside the spallation crack during Li plating. **e**. magnified image from a(vi) showing where the grayscale values were determined for the spallation crack (red box) and different parts of the vertical crack (blue and yellow boxes) after passage of 1.0 mAh cm^{-2}. **f**. grayscale analysis showing the amount of lithium in the regions of the crack identified by the boxes after passage of 1.0 mAh cm^{-2}. The colours in the histogram plot correspond to the colours of the boxes in e. The error bars are determined as described in the Methods. There is no lithium in the lower region of the vertical crack (yellow) even after passage of 1.0 mAh cm^{-2} when the crack has formed across the entire electrolyte from plated to stripped electrode. Current density 1 mA cm^{-2}, cell pressure 1.5 MPa. The combination of a relatively low pressure and 1 mA cm^{-2} was employed because it was found to induce lithium penetration even in the 1st plating[29].

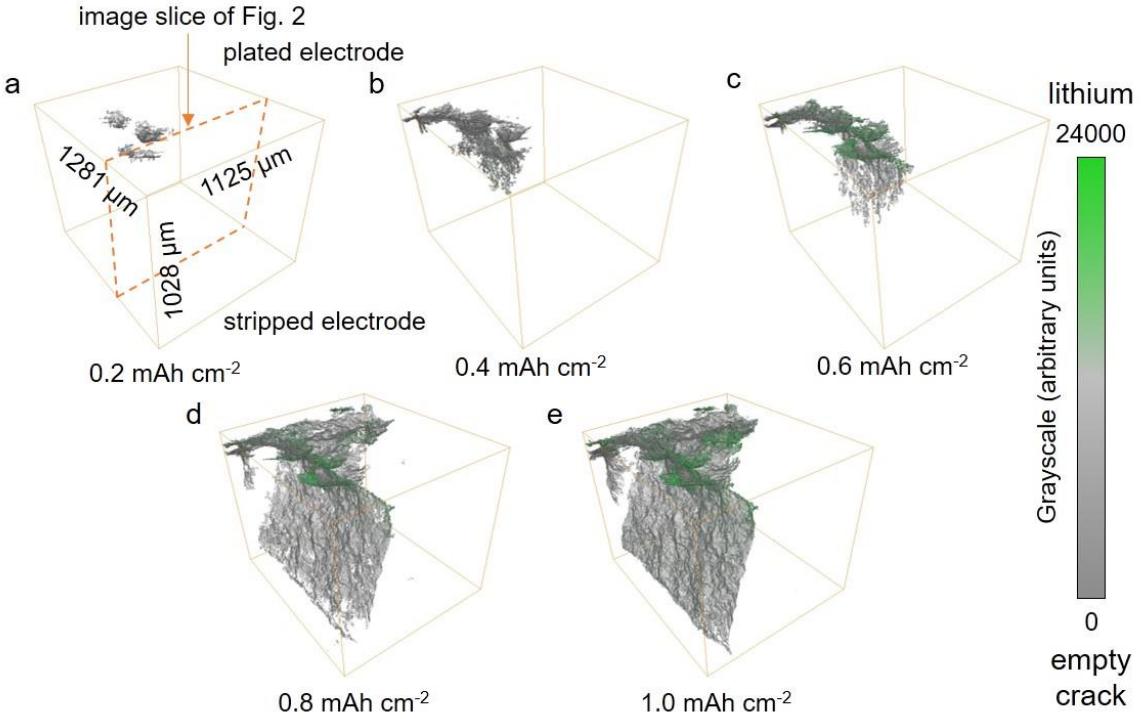

Fig. 4. 3D volume rendered images from the *in-situ* X-ray CT of cracks and deposited lithium inside the crack upon lithium plating, showing crack propagation ahead of lithium penetration. Rendering of a segment of the cell (approx., 1x1x1 mm^3) after: a. 0.2 mAh cm^{-2}, b. 0.4 mAh cm^{-2}, c. 0.6 mAh cm^{-2}, d. 0.8 mAh cm^{-2} and e. 1.0 mAh cm^{-2} of charge passed. In this case grey represents the empty crack and green the lithium. The location of the virtual cross-section in Fig. 3a is shown by the orange dashed line in Fig. 4a. The crack formed across the entire electrolyte from plated (top surface) to stripped (bottom surface) electrode before being fully filled with Li. Crack propagation ahead of Li ingress is in accord with absence of a short-circuit even when the crack reaches the stripped electrode.

3D image rendering was employed to visualise the crack propagation and lithium ingress in all directions as charge was passed, Fig. 4. The results are presented by mapping the colour scale from grey to green, where grey represents regions with low X-ray attenuation (empty crack) and green lithium. Li ingress into the solid electrolyte leads to the formation of spallations near the top of the image (plated electrode) after the passage of 0.2 mAh cm^{-2} of charge, Fig. 4a. After 0.4 mAh cm^{-2} of charge, spallations proliferate and cracks propagate perpendicular to the plated electrode, emanating from below the spallation, Fig. 4b. After 0.4 mAh cm^{-2} of charge Li is confined to the top of the cracks. Fig. 4c shows that after 0.6 mAh cm^{-2} of charge, the vertical cracks propagate further and there is increased deposition of lithium inside the spallation cracks. Fig 4d and e demonstrate that after 0.8 and 1.0 mAh cm^{-2} the vertical crack propagates all the way to the stripped (bottom) electrode but there is no evidence of lithium at or near the crack tip, the Li is still confined to the rear (top) of the crack even after 1.0 mAh cm^{-2}. These results show that both the spallation and the subsequent vertical crack that propagates across the electrolyte propagate well ahead of the lithium ingress. This observation is contrary to the predictions of most modelling work that cracks only propagate when fully filled with lithium metal[44–48]. As such, these findings considerably narrow the possible mechanisms for dendrite growth through ceramic electrolytes.

Dendrite distribution in a cycled cell

Previous studies have suggested dendrites may be found most frequently at the electrode edges[22]. Given the above results, that show more spallations occur near the edge than within the central region of the electrode, that vertical cracks propagate from spallations across the electrolyte, it is interesting to map the location of the spallations and dendrites. To investigate this, synchrotron X-ray diffraction mapping was employed, Fig. 5. A Li/Li_6PS_5Cl/Li cell was cycled galvanostatically at a current density of 1.5 mA cm^{-2} and with a capacity of 1.0 mAh cm^{-2} until a short-circuit was observed after 5 cycles. The cell was then aligned such that the incident monochromatic X-ray beam was perpendicular to the Li/Li_6PS_5Cl interface, i.e. along a line between the two electrodes. Diffraction mapping was carried out by collecting diffraction patterns from each segment of a 40 × 40 grid, centred on the electrode, with a grid size of 100 × 100 μm^2 and no overlap, as shown in Fig. 5a. Diffraction patterns of the sample, collected from each segment of the grid along the path of the transmitted beam through the electrode and electrolyte, are sensitive to dendrite formation along the beam path.

Diffraction patterns collected from the edge and centre of the electrode, marked as the red and blue squares respectively in Fig. 5a, are presented in Fig. 5b (i) and (ii). The position of the most intense peak of lithium metal (the {110} peak) is identified with a ✦. Whereas the peak is negligible in the pattern from the centre, it is strong at the edge of the electrode. Taking this peak intensity from each XRD pattern and plotting it as a function of the position across the cell permits mapping of the lithium dendrite distribution, Fig. 5c. It is apparent that most of the dendrites are distributed along the electrode edge, with a single long dendrite (the longest spike) leading to the short-circuit of the cell.

To correlate the location of the lithium dendrites that propagate across the electrolyte with the spallations, XCT was performed on the same cell. Fig. 5d (i) and (ii) show the image slices taken from the electrolyte along planes parallel and adjacent to the two Li/Li_6PS_5Cl interfaces.

To compare the dendrite distribution in Fig. 5c with the location of the spallations, the results of the diffraction mapping from Fig. 5c were superposed in 2D onto the XCT image slices in Fig. 5d. The colour scale is the same as in Fig. 5c, i.e. green represents low lithium intensity. ★ and ☆ mark the positions of the most intense peaks of lithium. Fig. 5d shows that although not all spallations are associated with lithium dendrites that propagate far into the electrolyte, but all such dendrites are associated with spallations. These results demonstrate that the observations in Fig. 3 and 4 are typical of how lithium dendrites penetrate the ceramic electrolyte and form short-circuits, i.e. Li ingress forms spallations at the plated electrode predominantly at the edges and lead to transverse cracks across the electrolyte that are increasingly filled with Li. The prevalence of spallations and dendrites at the edges of the electrode may be associated with enhanced electric fields and current densities at electrode edges, as reported in previous modelling and observations[22,49]. In addition, we also observed that some spallations and lithium dendrites form away from the edges of electrode, Fig. 5d. We attribute this to the regions of inferior contact (voids) between the lithium electrode and the electrolyte, which also results in enhanced electric fields and current densities. The higher current density at the edges and around voids is confirmed by the finite element analysis of current density across the cell in Fig. S8. The calculations are described in the SI.

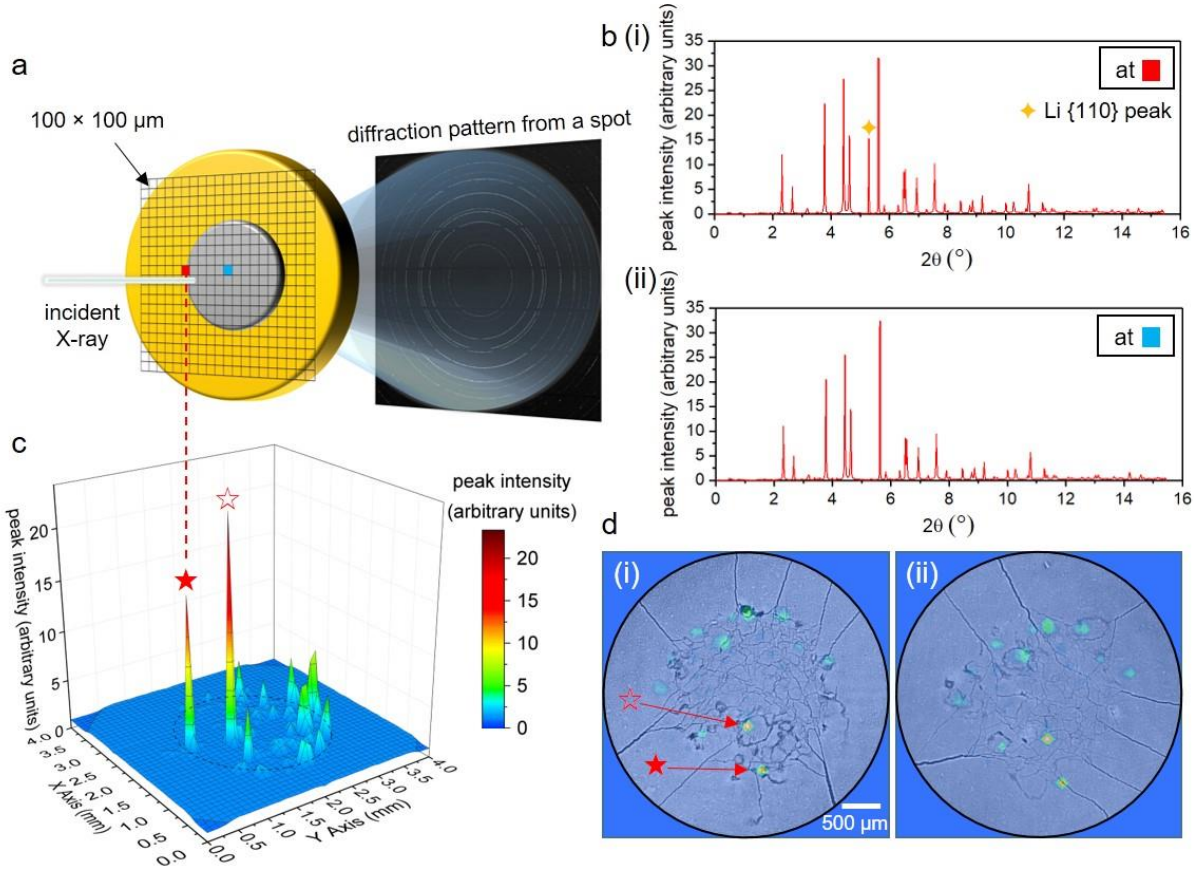

Fig. 5. Diffraction mapping showing distribution of lithium dendrites preferentially at the electrode edges and their association with the spallation cracks. Data collected on the Li/Li_6PS_5Cl/Li cell cycled at 1.5 mA cm^{-2} and capacity of 1 mAh cm^{-2} at 7 MPa pressure for 5 cycles until a short circuit occurred. **a**. schematic of X-ray diffraction mapping employing a 40 x 40 grid, with each grid segment being 100 x 100 μm^2 and no overlap. **b**. X-ray diffraction

data collected at (i) the edge and (ii) the centre of the electrode. ✦ identifies the lithium {110} peak, which is strong at the electrode edge (from grid segment shown in red) and not detectable at the centre (grid segment shown in blue). **c**. diffraction intensity of lithium {110} peak plotted at each grid position revealing the distribution of lithium dendrites. The dashed black circle marks the position of the electrodes in the cell. **d**. XCT image slices from planes in the electrolyte parallel and adjacent to the two electrodes. The location of the dendrites from the diffraction mapping have been superposed on these images (highlighted in green and yellow where green represents low intensity as in Fig. 5c). The two most intense lithium peaks are marked with ★ and ☆.

Correlation between spallation cracking and local porosity

Recent modelling work has postulated that porosity may have a role in dendrite growth and cross-sectional SEM images have shown lithium dendrites growing through pores[48,50,51]. Since the results presented here show that the formation of spallations leads to cracking that propagates across the electrolyte, it is interesting to examine the relationship between the spallations and the pre-existing porosity in the electrolyte.

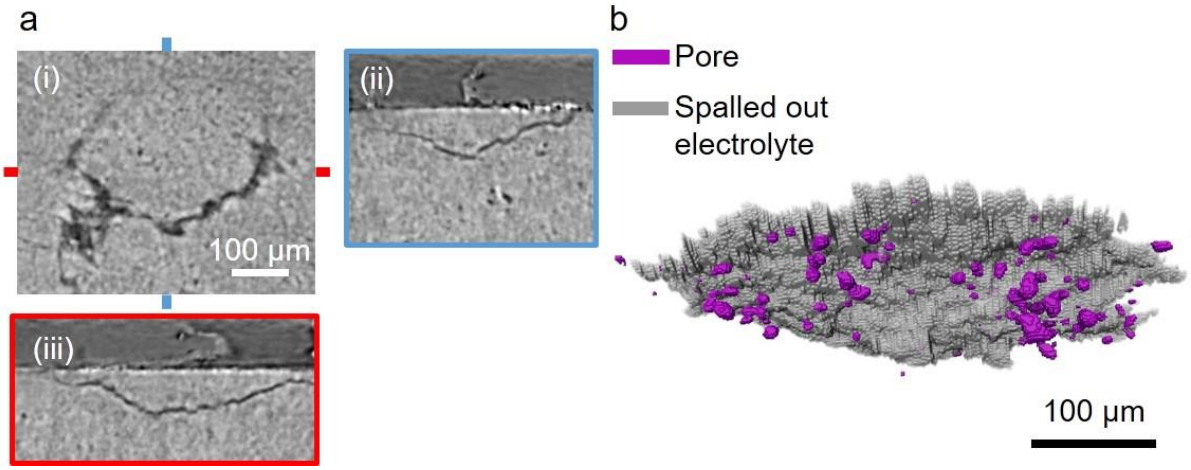

Fig. 6. Slices and volume rendered image from *in-situ* X-ray CT revealing the correlation between spallation and pre-existing pores inside the electrolyte. a. spallation imaged by XCT (i) parallel and adjacent to the plated electrode and (ii) and (iii) two virtual cross-sectional views. **b**. the spalled electrolyte is segmented out, rendered and shown in grey, with the pores present in the pristine electrolyte within the cracking region shown in purple.

A large spallation at the Li/Li_6PS_5Cl interface after plating is shown in Fig. 6a, with virtual slices taken in the electrolyte (i) parallel and adjacent to the plated lithium electrode and (ii) and (iii) two virtual cross-sectional views taken along the blue and red lines in (i). The spalled electrolyte was segmented out and rendered as shown in Fig. 6b. By superimposing the pore distribution in the pristine electrolyte onto the volume rendered image of the spalled electrolyte, it is apparent that there is significant porosity along the crack surface. The pore volumetric density is 4.12 % in the cracking region compared with 1.55 % for the bulk electrolyte, confirming the propensity for spallation to propagate along pre-existing pores. The volumetric

porosities derived from tomographic analysis excludes pores smaller than 3 × 3 × 3 voxels (voxel size 1.63 µm) because they cannot be identified with certainty. As a result, the total pore density in the region of the spallation will be higher than is seen in Fig. 6b.

Conclusions

In-situ phase-contrast X-ray CT combined with spatially mapped X-ray diffraction on Li/ Li_6PS_5Cl/Li cells, has been employed to investigate the propagation of cracks and the propagation of lithium through the solid electrolyte during plating. We show that cracks propagate through the electrolyte far ahead of the lithium dendrites, rather than lithium metal driving the crack tip forward. We demonstrate that Li ingress on plating results in the formation of spallation cracks (pot holes) adjacent to the interface with the plated electrode. Such cracks form because crack propagation to the nearest surface (the plated electrode) relieves the stress. The spallation crack propagates along a path where porosity is above the average of the ceramic. Spallations are more prevalent around the edge of the lithium electrode, where the field is greater, than elsewhere. Transverse cracks then form from the spallations and propagate across the electrolyte to the stripped electrode. Continued Li ingress widens the cracks and drives their propagation, but from the rear not the crack tip. The absence of short-circuits even when a crack traverses the entire electrolyte, linking the plated and stripped electrodes, supports the observation that lithium only later fills the crack completely. Our findings provide important insights into electrolyte cracking and lithium dendrite growth and hence the process of failure in all-solid-state batteries. They also suggest focussing more attention on blocking dry crack propagation to block dendrite propagation, for example by ceramic toughening and crack blocking, including strategies such as fibre reinforcement and transformation toughening.

References

1. Janek, J. & Zeier, W. G. A solid future for battery development. *Nature Energy* **1**, 1–4 (2016).
2. Pellegrini, V., Bodoardo, S., Brandell, D. & Edström, K. Challenges and perspectives for new material solutions in batteries. *Solid State Commun.* **303**–**304**, 113733 (2019).
3. Palacín, M. R. Recent advances in rechargeable battery materials: A chemist's perspective. *Chem. Soc. Rev.* **38**, 2565–2575 (2009).
4. Famprikis, T., Canepa, P., Dawson, J. A., Islam, M. S. & Masquelier, C. Fundamentals of inorganic solid-state electrolytes for batteries. *Nature Materials* **18**, 1278–1291 (2019).
5. Fincher, C. D., Ojeda, D., Zhang, Y., Pharr, G. M. & Pharr, M. Mechanical properties of metallic lithium: from nano to bulk scales. *Acta Mater.* **186**, 215–222 (2020).
6. Yang, C. *et al.* Continuous plating/stripping behavior of solid-state lithium metal anode in a 3D ion-conductive framework. *Proc. Natl. Acad. Sci. U. S. A.* **115**, 3770–3775 (2018).
7. Masias, A., Felten, N., Garcia-Mendez, R., Wolfenstine, J. & Sakamoto, J. Elastic, plastic, and creep mechanical properties of lithium metal. *J. Mater. Sci.* **54**, 2585–2600 (2019).
8. Han, F., Yue, J., Zhu, X. & Wang, C. Suppressing Li Dendrite Formation in Li2S-P2S5 Solid Electrolyte by LiI Incorporation. *Adv. Energy Mater.* **8**, 1703644 (2018).
9. Porz, L. *et al.* Mechanism of Lithium Metal Penetration through Inorganic Solid Electrolytes. *Adv. Energy Mater.* **7**, 1–12 (2017).
10. Lotsch, B. V. & Maier, J. Relevance of solid electrolytes for lithium-based batteries: A realistic view. *J. Electroceramics* **38**, 128–141 (2017).
11. Pang, Q., Liang, X., Shyamsunder, A. & Nazar, L. F. An In Vivo Formed Solid Electrolyte Surface Layer Enables Stable Plating of Li Metal. *Joule* **1**, 871–886 (2017).
12. Kerman, K., Luntz, A., Viswanathan, V., Chiang, Y.-M. & Chen, Z. Review—Practical Challenges Hindering the Development of Solid State Li Ion Batteries. *J. Electrochem. Soc.* **164**, A1731–A1744 (2017).
13. LePage, W. S. *et al.* Lithium Mechanics: Roles of Strain Rate and Temperature and Implications for Lithium Metal Batteries. *J. Electrochem. Soc.* **166**, A89–A97 (2019).
14. Chen, Y. *et al.* Li metal deposition and stripping in a solid-state battery via Coble creep. *Nature* **578**, 251–255 (2020).
15. van den Broek, J., Afyon, S. & Rupp, J. L. M. Interface-Engineered All-Solid-State Li-Ion Batteries Based on Garnet-Type Fast Li+ Conductors. *Adv. Energy Mater.* **6**, 1600736 (2016).
16. Monroe, C. & Newman, J. The Effect of Interfacial Deformation on Electrodeposition Kinetics. *J. Electrochem. Soc.* **151**, A880 (2004).
17. Monroe, C. & Newman, J. The Impact of Elastic Deformation on Deposition Kinetics at Lithium/Polymer Interfaces. *J. Electrochem. Soc.* **152**, A396 (2005).
18. Sharafi, A., Meyer, H. M., Nanda, J., Wolfenstine, J. & Sakamoto, J. Characterizing the Li-Li7La3Zr2O12 interface stability and kinetics as a function of temperature and current density. *J. Power Sources* **302**, 135–139 (2016).

19. Marbella, L. E. *et al.* 7 Li NMR Chemical Shift Imaging to Detect Microstructural Growth of Lithium in All-Solid-State Batteries. *Chem. Mater.* **31**, 2762–2769 (2019).
20. Aguesse, F. *et al.* Investigating the dendritic growth during full cell cycling of garnet electrolyte in direct contact with Li metal. *ACS Appl. Mater. Interfaces* **9**, 3808–3816 (2017).
21. Wu, B. *et al.* The role of the solid electrolyte interphase layer in preventing Li dendrite growth in solid-state batteries †. *Enegy Environ. Sci.* 1803–1810 (2018). doi:10.1039/c8ee00540k
22. Swamy, T. *et al.* Lithium metal penetration induced by electrodeposition through solid electrolytes: Example in single-crystal Li6La3ZrTaO12 garnet. *J. Electrochem. Soc.* **165**, A3648–A3655 (2018).
23. Kazyak, E. *et al.* Li Penetration in Ceramic Solid Electrolytes: Operando Microscopy Analysis of Morphology, Propagation, and Reversibility. *Matter* **2**, 1–24 (2020).
24. Manalastas, W. *et al.* Mechanical failure of garnet electrolytes during Li electrodeposition observed by in-operando microscopy. *J. Power Sources* **412**, 287–293 (2019).
25. Tippens, J. *et al.* Visualizing Chemomechanical Degradation of a Solid-State Battery Electrolyte. *ACS Energy Lett.* **4**, 1475–1483 (2019).
26. Seitzman, N. *et al.* Toward all-solid-state lithium batteries: Three-dimensional visualization of lithium migration in β-Li3PS4 ceramic electrolyte. *J. Electrochem. Soc.* **165**, A3732–A3737 (2018).
27. Doux, J. *et al.* Stack Pressure Considerations for Room Temperature All-Solid-State Lithium Metal Batteries. *Adv. Energy Mater.* 1903253 (2019). doi:10.1002/aenm.201903253
28. Spencer Jolly, D. *et al.* Sodium/Na β″ Alumina Interface: Effect of Pressure on Voids. *ACS Appl. Mater. Interfaces* **12**, 678–685 (2020).
29. Kasemchainan, J. *et al.* Critical stripping current leads to dendrite formation on plating in lithium anode solid electrolyte cells. *Nat. Mater.* **18**, 1105–1111 (2019).
30. Cao, C. *et al.* Emerging X-ray imaging technologies for energy materials. *Materials Today* (2019). doi:10.1016/j.mattod.2019.08.011
31. Boulineau, S., Courty, M., Tarascon, J. M. & Viallet, V. Mechanochemical synthesis of Li-argyrodite Li 6PS 5X (X = Cl, Br, I) as sulfur-based solid electrolytes for all solid state batteries application. *Solid State Ionics* **221**, 1–5 (2012).
32. Zhou, L. *et al.* Solvent-Engineered Design of Argyrodite Li 6 PS 5 X (X = Cl, Br, I) Solid Electrolytes with High Ionic Conductivity. *ACS Energy Lett.* **4**, 265–270 (2019).
33. Wenzel, S., Sedlmaier, S. J., Dietrich, C., Zeier, W. G. & Janek, J. Interfacial reactivity and interphase growth of argyrodite solid electrolytes at lithium metal electrodes. *Solid State Ionics* **318**, 102–112 (2018).
34. Yu, C., van Eijck, L., Ganapathy, S. & Wagemaker, M. Synthesis, structure and electrochemical performance of the argyrodite Li6PS5Cl solid electrolyte for Li-ion solid state batteries. *Electrochim. Acta* **215**, 93–99 (2016).
35. Lee, H. *et al.* Advances and Prospects of Sulfide All-Solid-State Lithium Batteries via One-to-One Comparison with Conventional Liquid Lithium Ion Batteries. *Advanced Materials* **31**, 1900376 (2019).

36. Krauskopf, T. *et al.* Lithium-Metal Growth Kinetics on LLZO Garnet-Type Solid Electrolytes. *Joule* **3**, 2030–2049 (2019).
37. Albertus, P., Babinec, S., Litzelman, S. & Newman, A. Status and challenges in enabling the lithium metal electrode for high-energy and low-cost rechargeable batteries. *Nat. Energy* **3**, 16–21 (2018).
38. Wenzel, S. *et al.* Interfacial Reactivity Benchmarking of the Sodium Ion Conductors Na3PS4 and Sodium β-Alumina for Protected Sodium Metal Anodes and Sodium All-Solid-State Batteries. *ACS Appl. Mater. Interfaces* **8**, 28216–28224 (2016).
39. Zhu, Y., He, X. & Mo, Y. Origin of Outstanding Stability in the Lithium Solid Electrolyte Materials: Insights from Thermodynamic Analyses Based on First-Principles Calculations. *ACS Appl. Mater. Interfaces* **7**, 23685–23693 (2015).
40. Bay, B. K., Smith, T. S., Fyhrie, D. P. & Saad, M. Digital volume correlation: Three-dimensional strain mapping using x-ray tomography. *Exp. Mech.* **39**, 217–226 (1999).
41. Eastwood, D. S. *et al.* Lithiation-induced dilation mapping in a lithium-ion battery electrode by 3D X-ray microscopy and digital volume correlation. *Adv. Energy Mater.* **4**, 1300506 (2014).
42. Pietsch, P. & Wood, V. X-Ray Tomography for Lithium Ion Battery Research: A Practical Guide. *Annu. Rev. Mater. Res* **471229**, 1–12 (2017).
43. Baruchel, J., Buffière, J. Y., Maire, E., Merle, P. & Peix, G. X-ray tomography in material science. *Hermes Sci. Publ.* **31**, 1–209 (2000).
44. Porz, L. *et al.* Mechanism of Lithium Metal Penetration through Inorganic Solid Electrolytes. *Adv. Energy Mater.* **7**, 1701003 (2017).
45. Athanasiou, C. E., Jin, M. Y., Ramirez, C., Padture, N. P. & Sheldon, B. W. High-Toughness Inorganic Solid Electrolytes via the Use of Reduced Graphene Oxide. *Matter* **3**, 212–229 (2020).
46. Klinsmann, M., Hildebrand, F. E., Ganser, M. & McMeeking, R. M. Dendritic cracking in solid electrolytes driven by lithium insertion. *J. Power Sources* **442**, 227226 (2019).
47. Bucci, G. & Christensen, J. Modeling of lithium electrodeposition at the lithium/ceramic electrolyte interface: The role of interfacial resistance and surface defects. *J. Power Sources* **441**, 227186 (2019).
48. Barroso-Luque, L., Tu, Q. & Ceder, G. An Analysis of Solid-State Electrodeposition-Induced Metal Plastic Flow and Predictions of Stress States in Solid Ionic Conductor Defects. *J. Electrochem. Soc.* **167**, 020534 (2020).
49. Tang, M., Albertus, P. & Newman, J. Two-Dimensional Modeling of Lithium Deposition during Cell Charging. *J. Electrochem. Soc.* **156**, A390 (2009).
50. Ren, Y., Shen, Y., Lin, Y. & Nan, C. W. Microstructure Manipulation for Enhancing the Resistance of Garnet-Type Solid Electrolytes to 'short Circuit' by Li Metal Anodes. *ACS Appl. Mater. Interfaces* **11**, 5928–5937 (2019).
51. Shen, F., Dixit, M. B., Xiao, X. & Hatzell, K. B. Effect of Pore Connectivity on Li Dendrite Propagation within LLZO Electrolytes Observed with Synchrotron X-ray Tomography. *ACS Energy Lett.* **3**, 1056–1061 (2018).
52. Paganin, D., Mayo, S. C., Gureyev, T. E., Miller, P. R. & Wilkins, S. W. Simultaneous phase and amplitude extraction from a single defocused image of a homogeneous object. *J. Microsc.* **206**, 33–40 (2002).

53. Marone, F. & Stampanoni, M. Regridding reconstruction algorithm for real-time tomographic imaging. *J. Synchrotron Radiat.* **19**, 1029–1037 (2012).

Methods

Synthesis of Li_6PS_5Cl

All procedures were performed inside an Ar-filled glovebox (O_2 and H_2O levels < 1 ppm). Li_2S, P_2S_5, and LiCl (Sigma-Aldrich) were ground together in the ratio corresponding to the stoichiometry of Li_6PS_5Cl. 1 g of such powder was then loaded into a ZrO_2 ball-mill jar with 50 g of 10-mm-diameter ZrO_2 balls. Two such sealed jars were removed from the glove box and placed in a Fritsch PULVERISETTE 7 premium line Planetary Micro Mill and ball-milled at 600 r.p.m. for 14 h. The ball-milled powder was then returned to the glove box and pressed into a disk with a 5-mm-diameter stainless steel die set under a uniaxial load of 1 t. The disk was placed onto graphite foil inside a preheated furnace at 600 °C (also in the glove box), then left to cool to room temperature. The disk was then ground with a mortar and pestle, pressed into a 5-mm-diameter disk at a uniaxial load of 1 t, and heated inside the furnace at 300 °C for 15 min. The sintered electrolyte disk was cooled to room temperature and used to assemble the cells.

Powder X-ray diffraction

Powder X-ray diffraction was carried out using a Rigaku Miniflex X-ray diffractometer with Cu $K_{\alpha1}$ radiation inside an N_2-filled glovebox, with O_2 and H_2O levels < 1 ppm.

Li/ Li_6PS_5Cl/Li symmetric cell assembly and cycling

Metallic lithium foil of 50 µm thick was punched into two 2-mm-diameter disk-shaped lithium electrodes, and pressed onto both sides of a sintered Li_6PS_5Cl disk. An insulating polymer ring was placed around the lithium to constrain and define the footprint of the lithium electrodes. All galvanostatic cycling was performed using a Gamry Reference 600+ potentiostat, with cells controlled under a defined stack-pressure. High current densities and resultant high overpotentials were used to initiate dendrite growth and electrolyte cracking.

Cross-sectional SEM

The two-electrode cells were cross-sectioned using an ultrasonic cutter with a tungsten carbide blade (SONOTEC) inside an Ar-filled glovebox. The cross-sectioned cells were mounted onto a custom-made holder with Cu adhesive tape and transferred into a Zeiss Merlin scanning electron microscope using an airtight transfer device (Gatan).

In-situ phase-contrast Synchrotron X-ray CT

X-ray tomograms were recorded at the TOMCAT beamline at the Swiss Light Source, Paul Scherrer Institute. The beam was monochromatized to 35 keV. Images were collected with a PCO Edge 5.5 sCMOS camera combined with an optical microscope with a x4 magnification, leading to a pixel size of 1.63 µm and a field of view of 4.2 × 3.5 mm^2. The conversion from X-

ray to visible light was achieved with a LuAG:CE 100 μm thick scintillator. The detector was placed at 350 mm from the sample, in order to work in propagation-based phase contrast. Exposure time was set to 200 ms. For each tomogram, 3570 equiangularly distributed projections were taken over 180° as well as 30 darks and 50 flats before and after the tomography scan. The projections were reconstructed using the Paganin phase retrieval method[52] and Gridrec reconstruction routines developed at the beamline[53].
X-ray tomograms were obtained at pristine, and after each step of electrochemical operation, where the electrochemical charge/discharge was paused to avoid possible image blurring due to morphological changes during tomogram collection.

***In-situ* Synchrotron X-ray CT-diffraction mapping**

The *in-situ* Synchrotron X-ray CT-diffraction mapping measurements were conducted at the I12 X-ray imaging and diffraction beamline, at the Diamond Light Source. The sample was mounted onto the sample stage with the incident X-ray perpendicular to the electrode. The tomogram was recorded at a monochromatic beam energy of 54 keV. For the tomogram, 2900 equiangularly distributed projections were taken over 180°, with the resulting voxel size of 3.24 μm and field of view of 8.0 × 7.0 mm^2. After the CT scan, the imaging detector was exchanged for a 2D area diffraction detector without moving the sample. Diffraction in transmission was then performed with the same monochromatic 54 keV beam, reduced by slits to a spot size of 100 × 100 $μm^2$ to map an area of 4 × 4 mm^2 with no overlap (a 40 × 40 matrix centred at the centre of lithium electrode). The diffraction data were analysed using the DAWN platform.

Analysis of grayscale in the crack

The grayscale values across the cracks were measured along a line perpendicular to the crack to confirm a continuous grayscale. Grayscale analysis was only taken where the crack is sufficiently wide (narrowest > 7 voxels) (1.63 μm/voxel and resolution 2× voxel size), to avoid potential effects from the surrounding electrolyte, and to assure reliable detection of lithium.
The grayscale values inside the crack at different regions (Fig. 3f) were measured and averaged along a 15-pixel line at the centre of the crack, parallel to the edge of the crack. The standard deviations of the grayscale values are given as error bars in the figure.

Electrochemical impedance spectroscopy measurements

Electrochemical impedance spectroscopy (EIS) was performed on two-electrode cells at a voltage perturbation of 10 mV, in a frequency range from 0.1 MHz to 0.1 Hz using a Gamry Reference 600+ potentiostat. The data were analysed using the ZView software package.

Analysis of Pore Volumetric Density

The analysis of pore volumetric density was conducted using Avizo Fire (ThermoFisher Scientific). The pore volumetric density of bulk electrolyte was calculated by greyscale segmentation of the pores in a cube of 500 × 500 × 500 voxels, with the pores below 3 × 3 × 3 voxels filtered out, and dividing the total volume of pores by the volume of the 500 × 500 × 500 voxel cube. The pore volumetric density along the spallation crack was calculated by segmenting out the pores which pre-existed in the pristine electrolyte and were crossed by the

spallation crack after 1st plating, with the pores below 3 × 3 × 3 voxels filtered out, and dividing the total volume of pores by the volume of the spallation cracking region.

Ex-Situ X-ray CT

The *ex-situ X-ray CT scans* on a cycled Na/Na-beta''-alumina symmetric cell (Fig. S3) and a cycled Li/Li_3N symmetric cell (Fig. 1d and Fig. S4) were obtained with a Zeiss Xradia Versa 510 X-ray computed tomography microscope. For the Na/Na-beta''-alumina symmetric cell, the tomogram was recorded at 120 kV accelerating voltage (current of 84 μA), with 3201 equiangularly distributed projections over 360°, resulting in a voxel size of 4.67 μm and field of view of 9.37 × 9.56 mm^2. For the Li/Li_3N symmetric cell, the tomogram was recorded at 40 kV accelerating voltage (current of 74 μA), with 1601 equiangularly distributed projections over 360°, resulting in a voxel size of 3.85 μm and field of view of 3.81 × 3.89 mm^2.

Acknowledgements

P.G.B. is indebted to the Faraday Institution All-Solid-State Batteries with Li and Na Anodes (FIRG007, FIRG008), as well as the Engineering and Physical Sciences Research Council (EPSRC), Enabling Next Generation Lithium Batteries (EP/M009521/1), the University of Oxford experimental equipment upgrade (EP/M02833X/1) and the Henry Royce Institute for capital equipment (EP/R010145/1) for financial support. G. L. and C. W. M. acknowledge financial support by the Faraday Institution Multiscale Modelling (FIRG003) and the UK Industrial Strategy Challenge Fund: Materials Research Hub for Energy Conversion, Capture, and Storage (M-RHEX), under grant (EP/R023581/1). The authors thank Paul Scherrer Institut, Villigen, Switerland, and Diamond Light Source, Harwell, UK for provision of synchrotron radiation beamtime (Experiment number 20182142) at the TOMCAT beamline X02DA of the SLS, and beam time (Experiment number EE20795-1) at the I12 beamline of the DLS. We acknowledge technical and experimental support at the TOMCAT by Dr. Anne Bonnin and Dr. Johannes Ihli, at the I12 by Dr. Oxana Magdysyuk.

Author contributions

Z.N. contributed to all aspects of the research. Z.N., D.S.J., J.I., and A.B. carried out the *in-situ* phase-contrast synchrotron X-ray CT. Z.N., D.S.J., R.D.M., S.D.P., Y.C., and O.M. carried out the *in-situ* synchrotron X-ray CT-diffraction mapping. Z.N. and J.K. performed synthesis of Li_6PS_5Cl and PXRD characterization. Z.N. and S.D.P. performed the SEM experiment. G.L. and C.W.M. conducted the finite element analysis of current density distribution. Z.N., D.S.J., R.D.M., S.D.P., Y.C., C.G., B.L., P.A., D. M., G.O.H., T.J.M., and P.G.B. interpreted the data. Z.N. and P.G.B. wrote the manuscript with contributions and revisions from all authors. The project was supervised by T.J.M. and P.G.B.